Transactions on Materials, Biotechnology and Life Sciences
ISSN: 2960-1932, eISSN: 2960-2319 | Volume 8
MMTCS 2025

Development of a PLA-*b*-PEG Drug Delivery Carrier Design Framework and ROS pH Responsive Methotrexate Carriers for RA

Jiaxuan (Joseph) Fu *

Hangzhou International School, Hangzhou China

* Corresponding Author Email: jfu080111@gmail.com

Abstract. Methotrexate (MTX) remains the first-line treatment for rheumatoid arthritis (RA), but its clinical use faces substantial challenges due to poor water solubility and systemic side effects. To address these limitations, this study develops a framework for designing polymer-based drug delivery carriers by investigating the relationship between polymer parameters, self-assembly behavior, and pharmacokinetic properties of PLA-*b*-PEG block copolymers. A multiparameter analysis examined the effects of block ratio, crystallinity (PLLA vs. PDLLA), polymer architecture (triblock vs. 4-arm), and solvent conditions on nanoaggregate morphology and drug release kinetics. Six PLA-*b*-PEG copolymers were synthesized and characterized using ^{1}H NMR, GPC, and TEM. Self-assembly via co-solvent methods generated diverse morphologies, which were explained using critical packing parameter theory and Hansen solubility parameters. Drug loading efficiency ranged from 32.5% to 61.81%, with capacity reaching up to 18.54%. Release kinetics followed the Korsmeyer-Peppas model, revealing molecular weight-dependent trends. From these findings, a retrosynthetic design framework was established to link polymer parameters to desired therapeutic outcomes. Two optimized formulations were developed for RA treatment, $PLLA_{3.4k}$-PEG_{5k}-$PLLA_{3.4k}$ and 4-arm PEG_{5k}-$PLLA_{3.6k}$. Notably, the 4-arm architecture demonstrated better performance with 83.0% drug loading efficiency compared to 73.3% for linear. Both formulations responded synergistically to reactive oxygen species (ROS) conditions, demonstrating their ability to target inflamed locations (63.73% faster release under combined acidic pH 6.5/H_2O_2), and exhibited excellent biocompatibility (<0.3% hemolysis). Functionally, both formulations displayed significant anti-inflammatory efficacy, reducing key cytokines (TNF-α, IL-6, IL-1β) by 45-65% and promoting a shift in macrophage polarization from M1 to M2 phenotypes.

Keywords: Targeted Drug Delivery; Rheumatoid Arthritis; Methotrexate Treatment; Block Copolymer; Self-Assembly.

1. Introduction

Rheumatoid Arthritis (RA) is a chronic autoimmune disease with higher prevalence in females and the elderly, affecting 0.5–1% of the global population.[1] Methotrexate (MTX) is the standard treatment, often combined with other anti-rheumatic drugs, but its clinical use is limited by poor solubility and side effects including hepatotoxicity and myelosuppression.[2, 3] To overcome these issues, it is necessary to design carriers that can effectively deliver MTX into the inflamed joints.

Inflamed synovial tissues in RA present a pathological microenvironment characterized by elevated reactive oxygen species (ROS) and acidic pH (about 6.5), resulting from activated immune cells and hypoxia.[1, 4] These conditions provide opportunities for designing dual-responsive carriers capable of selective drug release.

Polymer-based nanocarriers have advanced modern therapeutics by enabling controlled pharmacokinetics, targeted delivery, and tunable release profiles.[5, 6] Loading drugs into these nanoaggregates can help resolve many of the issues drugs may face when directly administered, as they allow for precise control over pharmacokinetic profiles by tuning the characteristics of self-assembled nanoaggregates, especially size and shape.[7] Studies have indicated that variations in carrier size and morphology significantly influence pharmacokinetic properties, including cellular uptake, renal clearance, and half-life. Furthermore, nanoaggregate morphologies exhibit vastly

different release behaviors, which can be strategically utilized.[8, 9] Other functions, such as targeted and controlled release, can also be easily implemented due to their ease of synthesis and modification.[10] However, drug loading efficiency often remains below 10%, limiting clinical translation.[11]

Among various materials used to prepare polymer-based carriers, amphiphilic block copolymers (BCPs) are of interest for their unique physical and chemical properties. BCPs are particularly valued for their ability to self-assemble into diverse nanoaggregates with well-defined morphologies in an aqueous environment, a property that has been allowed for by finely-tuned polymer chemistry.[12] The self-assembly process of BCPs is essential for the development of advanced nanomaterials, with applications in areas such as biomedicine, membrane technology, and photonics.[13, 14] The assembly process is mainly driven by the free energy, enthalpy, and entropy changes within the system.[15]

For drug delivery applications, polylactic acid-block-polyethylene glycol (PLA-*b*-PEG) has emerged as a particularly promising BCP system. Both poly(lactic acid) (PLA) and poly(ethylene glycol) (PEG) offer biocompatible and biodegradable properties, making them ideal candidates for pharmaceutical applications.[16] While factors (ratios between hydrophobic and hydrophilic blocks, solvents used for self-assembly, and degrees of polymerization) that greatly influence the self-assembly of amphiphilic BCPs have been extensively investigated, a knowledge gap remains.

Previous studies have investigated the self-assembly behaviors of PLA-*b*-PEG in various conditions, and the applications of their self-assembled nanoaggregates mainly focused on the efficacy of hydrogels composed of PLA-*b*-PEG.[17, 18] Although multi-arm PLA-*b*-PEGs have been used and different topologies have been produced by changing their polymer properties, no study has understood their self-assembly in a controlled setting, where standard factors, along with the newly introduced architectural variable influencing self-assembly, are held consistent for accurate relationships to be constructed with one another, which could inform the design of tunable nanostructures. [19, 20]

This study addresses that gap by (i) conducting a systematic multiparameter analysis of PLA-*b*-PEG self-assembly, elucidating the hierarchy of factors governing morphology and drug release, and (ii) applying these insights to design ROS- and pH-responsive carriers for MTX delivery in RA. The resulting systems were characterized by DLS and TEM, evaluated for drug release under physiological and pathological conditions, and tested for safety and performance using hemolysis, cytotoxicity, macrophage activation, ELISA, and Western blot assays.

By linking polymer architecture to morphology and pharmacokinetics, this study establishes a retrosynthetic framework for PLA-*b*-PEG based drug delivery carriers. In addition, by utilizing the constructed framework and exploiting the unique pathological characteristics of RA, including elevated ROS levels and acidic pH, dual-responsive systems that can achieve synergistic targeting effects for highly selective drug release were developed.

2. Methods

2.1. Synthesis of PLA-*b*-PEG Block Copolymers

Block copolymers (BCPs) were synthesized by ring-opening polymerization of LLA or DLLA with PEG using Sn $(Oct)_2$ as catalyst under anhydrous conditions at 100 °C. Reaction progress was monitored by ^{1}H NMR (PLA at 5.2 ppm, PEG at 3.5 ppm). Target final peak for triblock $PLA_{2.5K}$-*b*-PEG_{5K}-*b*-$PLA_{2.5K}$ is 1:8, while for triblock PLA_{10K}-*b*-PEG_{5K}-*b*-PLA_{10K} is 1:2. For the 4-arm BCPs, $(PLA_{2.5K})_2$-*b*-PEG_{5K}-*b*-$(PLA_{2.5K})_2$ showed a peak ratio of 1:4. In contrast, $(PLA_{10K})_2$-*b*-PEG_{5K}-*b*-$(PLA_{10K})_2$ showed a peak ratio of 1:1. Products were purified by dissolution in dichloromethane and triple precipitation into cold methanol, followed by vacuum drying at 40 °C.

2.2. Preparation of Nanoaggregates and Drug Loading

Nanoaggregates were obtained by co-solvent self-assembly. BCPs (1 mg/mL in dioxane or THF) were mixed with water (3 mL, 1 mL/min) under stirring and dialyzed (MWCO 3500 Da, 24 h). For fluorescent tracking, FNa (0.1 mg/mL) was added during assembly.

For MTX loading, MTX (20 mg/mL in DMSO) was added dropwise (0.5 mL, 1 mL/min) into 10 mL of polymer solution (10 mg/mL), followed by dialysis under the same conditions. Drug loading efficiency was determined by fluorescence before and after dialysis. Release was studied by immersing dialysis bags in PBS (pH 6.5 or 7.4, 37 °C) and sampling at defined time points (0–24 h).

2.3. Hemocompatibility and Cytotoxicity Assays

Hemolysis was evaluated by incubating micelles (0.06–1 mg/mL) with a 2% rabbit RBC suspension at 37 °C for 2 h. After centrifugation, hemoglobin release was quantified at 540 nm, with 0.9% NaCl and water as negative and positive controls.

For cytotoxicity, RAW 264.7 and HUVEC cells were cultured in DMEM with 10% FBS and 1% Pen/Strep at 37 °C, 5% CO_2. Cells (~10,000/well) were plated in 96-well plates, exposed to MTX-containing medium for 24 h, and analyzed using the CCK-8 assay with absorbance at 450 nm.

2.4. Immunological Evaluation

Macrophage polarization was assessed by culturing ~100,000 RAW 264.7 cells in chambers, fixing, permeabilizing, and staining with iNOS (M1) or CD206 (M2) primary antibodies, followed by fluorescent secondaries and Hoechst nuclear stain. Imaging was done with confocal microscopy.

For protein expression, cells were lysed in RIPA buffer, and 15 μg of protein per sample was separated by SDS-PAGE and transferred to PVDF membranes. Membranes were probed with antibodies against β-actin, VCAM-1, PKB, or NF-κB, followed by HRP-conjugated secondaries. Bands were visualized by ECL and quantified with ImageJ.

Cytokine secretion was quantified by ELISA: clarified supernatants were incubated with capture antibody, biotinylated detection antibody, and streptavidin-HRP, followed by TMB substrate. Absorbance was measured at 450 nm.

2.5. Characterizations

^{1}H NMR confirmed polymer ratios; GPC determined Mn, Mw, and PDI. TEM visualized nanoaggregate morphology, DLS measured size distribution, and fluorescence spectroscopy quantified FNa/MTX release profiles.

3. Results

3.1. Aggregate Characteristics

3.1.1. Synthesis and Characterization of PLA-b-PEG Nanoaggregates

A series of PEG_m-*b*-PLA_n copolymers (where m and n represent the number of repeating units in the PEG and PLA blocks, respectively) was synthesized through ring-opening polymerization. The recrystallized LLA and DLLA monomers were mixed with anhydrous PEG-OH (used as the macroinitiator) and $Sn(Oct)_2$ (used as the catalyst). The polymerization reaction was initiated by raising the solution temperature to 100 °C, and terminated by lowering the temperature once the reaction reached completion. Two types of PEG were employed in the synthesis: triblock PEG and 4-arm PEG. Through this process, a total of six distinct PEG_m-*b*-PLA_n polymers were obtained.

When the triblock PEG is used, changing the ratio of added DLLA and PEG allows for the synthesis of two PDLLA-*b*-PEG BCPs with different block ratios. An introduction of crystallinity in the block of PLA was supposed to provide an additional parameter to control the self-assembly and morphology

of the nanoaggregates; instead of DLLA, LLA was used to synthesize another two PLLA-*b*-PEG BCPs. The same block ratios were achieved for PDLLA-*b*-PEG and PLLA-*b*-PEG to make these polymers comparable. To further investigate the effect of polymer architecture, 4-arm PEG was used to facilitate the synthesis of 4-arm PLA-*b*-PEG BCPs, allowing for more morphologies to be prepared. Two 4-arm PLLA-*b*-PEG were synthesized, which can be compared to triblock PLLA-*b*-PEG to evaluate the effect of block ratio and crystallinity.

The PEG block length was fixed at m = 113 since all of these polymers have the same PEG molecular weight of 5000 g/mol, and block ratio and weight percentage of PLA in each copolymer were determined using ^{1}H-NMR spectroscopy by analyzing the integral differences between the protons of PEG and PLA. The molecular weights and polydispersity indices (PDI) of the copolymers were measured by gel permeation chromatography (GPC). These results are summarized in **Table 1**. These polymers are denoted as $PDLLA_{4.7K}$-PEG_{5K}-$PDLLA_{4.7K}$, $PDLLA_{7.8K}$-PEG_{5K}-$PDLLA_{7.8K}$, $PLLA_{3.4K}$-PEG_{5K}-$PLLA_{3.4K}$, $PLLA_{6.8K}$-PEG_{5K}-$PLLA_{6.8K}$, 4-arm PEG_{5K}-$PLLA_{3.6K}$, and 4-arm PEG_{5K}-$PLLA_{12.6K}$.

Table 1. Molecular Weights and Basic Information of Polymers.

Polymer number	Materials	Molar Ratio	Molecular Weight		f_{PLA} (%)	*PDI*
			PEG	PLA		
1	$PDLLA_{4.7K}$-PEG_{5K}-$PDLLA_{4.7K}$	113/130	5000	9371	75.84	1.17
2	$PDLLA_{7.8K}$-PEG_{5K}-$PDLLA_{7.8K}$	113/217	5000	15698	57.49	1.04
3	$PLLA_{3.4K}$-PEG_{5K}-$PLLA_{3.4K}$	113/93	5000	6761	65.21	1.05
4	$PLLA_{6.8K}$-PEG_{5K}-$PLLA_{6.8K}$	113/189	5000	13625	73.15	1.35
5	4-arm PEG_{5K}-$PLLA_{3.6K}$	113/198	5000	14309	74.11	1.09
6	4-arm PEG_{5K}-$PLLA_{12.6K}$	113/697	5000	50272	90.95	1.17

3.1.2. Morphology Analysis by TEM

Once the polymers were synthesized, the effects of their parameters—block ratio, crystallinity, and architecture—on self-assembly were evaluated using the cosolvent method. The polymers were dissolved in common solvents (dioxane and THF), and water was added to induce aggregation. TEM analysis was then used to characterize the structures of these aggregates, revealing the effect of these parameters on self-assembly (**Figure 1**).

In dioxane, $PDLLA_{4.7K}$-PEG_{5K}-$PDLLA_{4.7K}$ gave spheres with a diameter of 100 nm, while $PDLLA_{7.8K}$-PEG_{5K}-$PDLLA_{7.8K}$ with a longer PDLLA chain resulted in 200 nm spheres, with smaller 50-100 nm spheres also observed (**Figure 1a-b**). Changing PDLLA to PLLA for short PLA chain BCP does not significantly alter the aggregate morphology, e.g., $PLLA_{3.4K}$-PEG_{5K}-$PLLA_{3.4K}$ formed similarly 200-400 nm spheres (**Figure 1c**). However, for $PLLA_{6.8K}$-PEG_{5K}-$PLLA_{6.8K}$ with a longer PLLA chain, large 2000 nm lozenge platelets were observed together with 200 nm spheres (**Figure 1d**). When architecture was modified, 4-arm PEG_{5K}-$PLLA_{3.6K}$ and 4-arm PEG_{5K}-$PLLA_{12.6K}$ formed 1000 nm cylinders with 200 nm spheres and 200 nm spheres during self-assembly, respectively, as shown in **Figure 1e-f**.

In THF, PDLLA-*b*-PEG showed similar morphologies to those in dioxane but with larger sizes, i.e., uniformly shaped 400 nm spheres for $PDLLA_{4.7K}$-PEG_{5K}-$PDLLA_{4.7K}$ and 300 to 700 nm spheres for $PDLLA_{7.8K}$-PEG_{5K}-$PDLLA_{7.8K}$ (**Figure 1g-h**). While $PLLA_{3.4K}$-PEG_{5K}-$PLLA_{3.4K}$ still gave a similar spherical structure, the $PLLA_{6.8K}$-PEG_{5K}-$PLLA_{6.8K}$ resulted in more complex structures, 2000 nm × 1000 nm dumbbells with 800 nm rings and 100 nm spheres, with the dumbbells and rings as the majority of the nanoaggregates (**Figure 1j**). THF does not significantly change the morphologies for

the different architectures of 4-arm polymers, with only small changes in the size and the addition of a dumbbell morphology. 4-arm PEG_{5K}-$PLLA_{3.6K}$ and 4-arm PEG_{5K}-$PLLA_{12.6K}$ formed 1000 nm cylinders, 2000 nm × 1000 nm dumbbells, and 100-400nm spheres, respectively (**Figure 1k-l**).

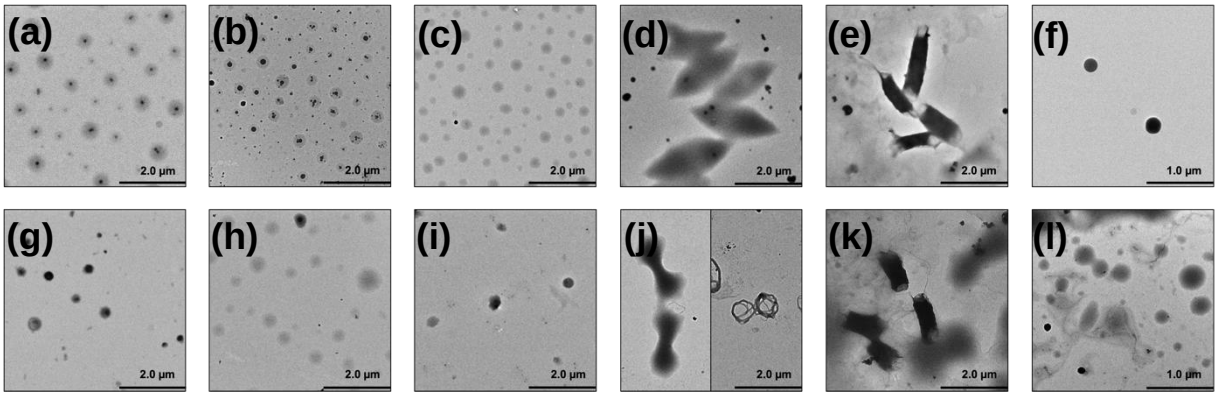

Figure 1. TEM images of self-assembled aggregates with different polymer structures and solvents. In dioxane: (a) $PDLLA_{4.7K}$-PEG_{5K}-$PDLLA_{4.7K}$; (b) $PDLLA_{7.8K}$-PEG_{5K}-$PDLLA_{7.8K}$; (c) $PLLA_{3.4K}$-PEG_{5K}-$PLLA_{3.4K}$; (d) $PLLA_{6.8K}$-PEG_{5K}-$PLLA_{6.8K}$; (e) 4-arm PEG_{5K}-$PLLA_{3.6K}$; (f) 4-arm PEG_{5K}-$PLLA_{12.6K}$. THF: (g) $PDLLA_{4.7K}$-PEG_{5K}-$PDLLA_{4.7K}$; (h) $PDLLA_{7.8K}$-PEG_{5K}-$PDLLA_{7.8K}$; (i) $PLLA_{3.4K}$-PEG_{5K}-$PLLA_{3.4K}$; (j) $PLLA_{6.8K}$-PEG_{5K}-$PLLA_{6.8K}$; (k) 4-arm PEG_{5K}-$PLLA_{3.6K}$; (l) 4-arm PEG_{5K}-$PLLA_{12.6K}$.

The morphological features across different polymers and solvents are summarized in **Table 2**.

Table 2. Polymer and Their Corresponding Formed Nanoaggregate Morphologies.

Polymer	Morphology in Dioxane	Morphology in THF
$PDLLA_{4.7K}$-PEG_{5K}-$PDLLA_{4.7K}$	100 nm spheres	400 nm spheres
$PDLLA_{7.8K}$-PEG_{5K}-$PDLLA_{7.8K}$	200 nm spheres, smaller 50-100 nm spheres	300-700 nm spheres
$PLLA_{3.4K}$-PEG_{5K}-$PLLA_{3.4K}$	200-400 nm spheres	400 nm spheres
$PLLA_{6.8K}$-PEG_{5K}-$PLLA_{6.8K}$	Large 2000 nm lozenge platelets, 200 nm spheres	2000 nm × 1000 nm dumbbells, 800 nm rings, 100 nm spheres
4-arm PEG_{5K}-$PLLA_{3.6K}$	1000 nm cylinders with 200 nm spheres	1000 nm cylinders, 2000 nm × 1000 nm dumbbells
4-arm PEG_{5K}-$PLLA_{12.6K}$	200 nm spheres	100-400 nm spheres

3.2. Aggregate Pharmacokinetics

3.2.1. Loading Efficiency and Loading Capacity

The loading efficiency of the polymers was determined by Eq. (1).

$$\frac{W_{loaded}}{W_{feed}} \times 100 \quad (1)$$

Once experimentation was conducted, I analyzed the loading efficiency and capacity. Results highlight the differences between nanoaggregates of different sizes and morphologies and how the release and loading behavior can be attributed to these two factors. From **Figure 2**, $PDLLA_{7.8K}$-PEG_{5K}-$PDLLA_{7.8K}$ exhibited the highest loading efficiency in THF (61.81%), while $PLLA_{3.4K}$-PEG_{5K}-$PLLA_{3.4K}$ demonstrated the highest loading efficiency in dioxane (55.04%). Conversely, 4-arm PEG_{5K}-$PLLA_{12.6K}$ showed the lowest loading efficiency in both solvents.

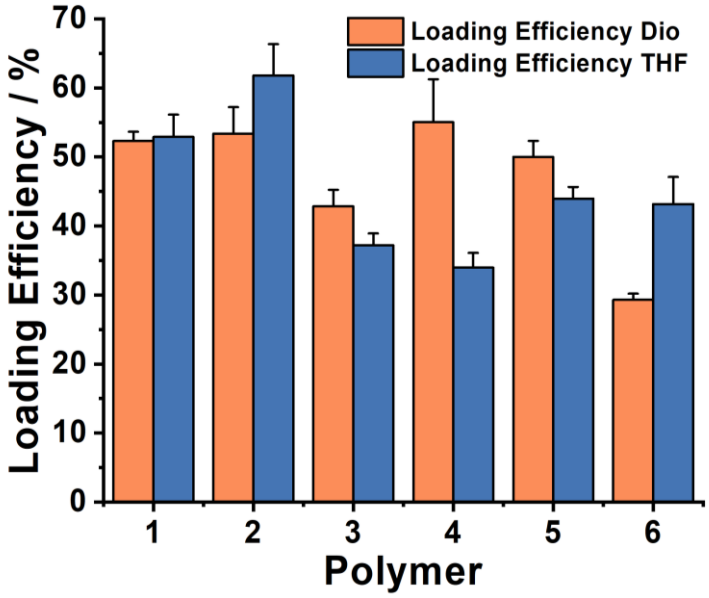

Figure 2. Graphical representation of loading efficiency and its corresponding nanoaggregates self-assembled under various conditions.

The loading capacity reflects the percentage of drug encapsulated relative to the total polymer weight, as defined in Eq. (2).

$$\frac{W_{loaded}}{W_{nanoaggregate}} \times 100 \quad (2)$$

Among the polymers, $PDLLA_{4.7K}$-PEG_{5K}-$PDLLA_{4.7K}$ showed the highest loading capacity in THF (18.54%), while $PLLA_{6.8K}$-PEG_{5K}-$PLLA_{6.8K}$ exhibited the highest loading capacity in dioxane (16.51%), as shown in **Figure 3**. Interestingly, 4-arm PEG_{5K}-$PLLA_{12.6K}$ had the lowest loading capacity in both solvents, with particularly low values in dioxane (8.79%) **(Figure 3)**.

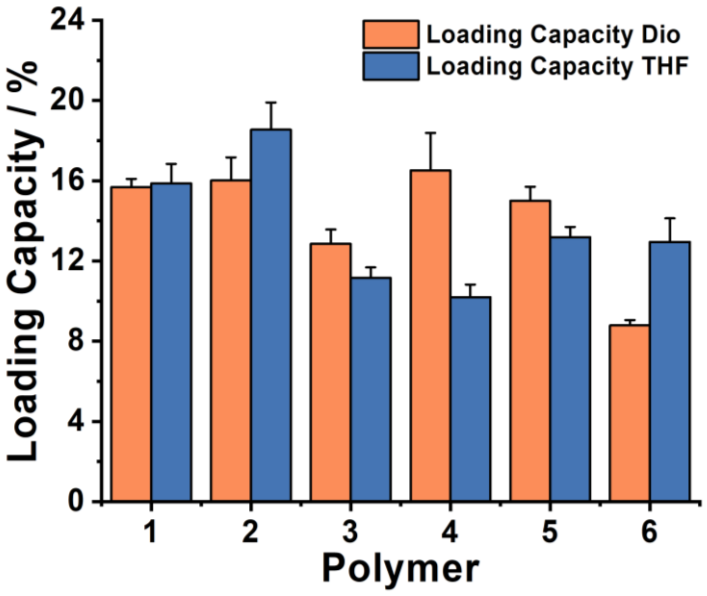

Figure 3. Graphical representation of loading capacity and its corresponding nanoaggregates self-assembled under various conditions

Korsmeyer Peppas Model:

$$\% \, Released = \frac{M_t}{M_\infty} = kt^n \tag{3}$$

M_t = mass of drug released at time t

M_∞= total mass of drug in the system

k = release constant

n = release exponent (indicative of the release mechanism)

3.2.2. Drug Release Profiles and Kinetics

The release kinetics data in **Table 3** were calculated from the data shown in **Figure 4** using the Korsmeyer Peppas model. The resulting values reveal how several competing factors influence drug release in these formulations. A clear molecular weight dependence is observed in the linear triblock copolymers, where increasing the hydrophobic block length consistently decreases the release rate constant (k) - for instance, $PDLLA_{4.7K}$-$PEG_{3.4K}$-$PDLLA_{4.7K}$ shows k values of 3.61 and 3.75 for Dio and THF, respectively, while $PDLLA_{7.8K}$-PEG_{5K}-$PDLLA_{7.8K}$ exhibits much lower values of 1.72 and 1.15 **(Table 3-4)**.

Table 3. Release kinetics of micelles.

Material	**Dio 7.4**		**THF 7.4**	
	k	n	k	n
$PDLLA_{4.7K}$-PEG_{5K}-$PDLLA_{4.7K}$	3.61	0.36	3.75	0.31
$PDLLA_{7.8K}$-PEG_{5K}-$PDLLA_{7.8K}$	1.72	0.54	1.15	0.46
$PLLA_{3.4K}$-PEG_{5K}-$PLLA_{3.4K}$	5.02	0.23	5.25	0.24
$PLLA_{6.8K}$-PEG_{5K}-$PLLA_{6.8K}$	0.99	0.66	2.92	0.47
4-arm PEG_{5K}-$PLLA_{3.6K}$	4.39	0.31	6.24	0.21
4-arm PEG_{5K}-$PLLA_{12.6K}$	13.37	0.43	9.64	0.39

Table 4. Table summarizing the release mechanism and its corresponding diffusion coefficient n.

n	Indication
Less than 0.45	Quasi Fickian
0.45	Fickian Diffusion
0.45<n<0.89	Anomalous Diffusion or Non-Fickian Diffusion
0.89<n<1	Case 2 Relaxation or Non Fickian Case II
1<n	Non-Fickian Super Case II

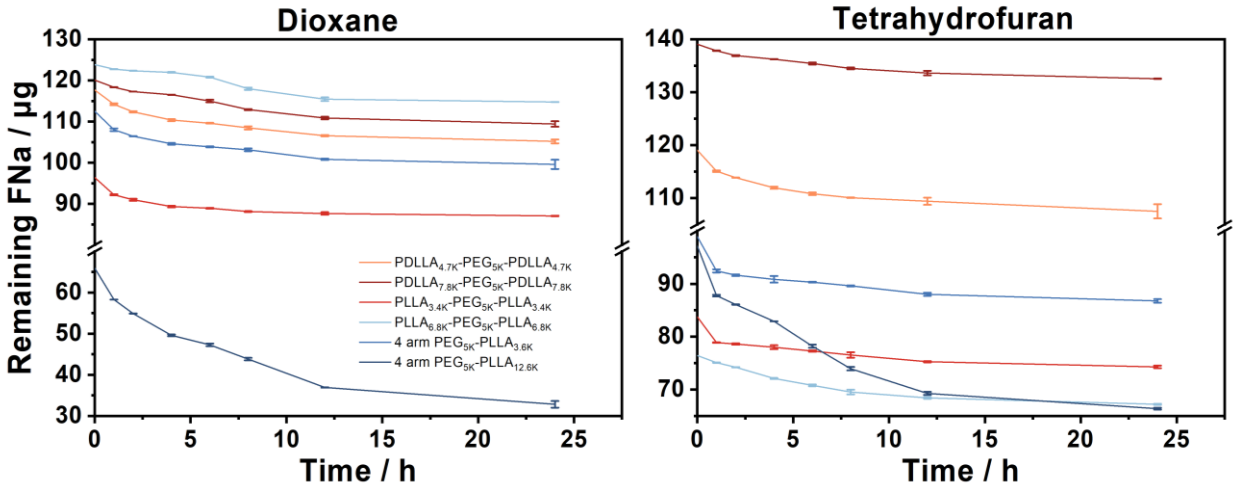

Figure 4. Drug release curves for aggregates synthesized from various polymers. Abbreviations in the key refer to the solvents used in self-assembly (dioxane and tetrahydrofuran). In vivo studies were conducted at pH 7.4.

The diffusion coefficient obtained through the Korsmeyer Peppas model, which indicates the release mechanism, exhibits a positive relationship with the length of the PLA chain **(Table 3-4).** $PDLLA_{7.8K}$-PEG_{5K}-$PDLLA_{7.8K}$ showed a higher diffusion coefficient in dioxane at pH 7.4 (0.54) than $PDLLA_{4.7K}$-PEG_{5K}-$PDLLA_{4.7K}$ (0.36), indicating the role of chain length in controlling release **(Table 3-4**).

3.3. Carrier Design and Evaluation

3.3.1. Methotrexate Loading in Selected Polymers

Based on the knowledge learned from the experimentation of the PLA-*b*-PEG polymer, $PLLA_{3.4K}$-PEG_{5K}-$PLLA_{3.4K}$ and 4-arm PEG_{5K}-$PLLA_{3.6K}$ were selected. Both exhibit relatively high release rates ($k \approx 4.39–6.24$), ensuring efficient drug delivery, while their low diffusion exponents ($n \approx 0.21–0.31$) indicate Fickian diffusion, meaning release is primarily controlled by diffusion rather than polymer swelling or erosion. This makes their release kinetics more predictable and stable, which is particularly advantageous at physiological pH (7.4), where sustained release is desirable for sustained inhibition of RA symptoms. In RA microenvironments (pH ~6.5, H_2O_2), where accelerated ROS and pH-triggered drug release is needed, the formulations would show greater, comparatively accelerated drug release rates between the normal human and RA microenvironment, allowing for rapid response to severe immune responses, quickly alleviating stress on the patient. In contrast, formulations with higher n values (e.g., Formulation 4, $n \approx 0.47–0.66$) exhibit anomalous or erosion-dependent release, which is less ideal under normal conditions, as the formulation would not further accelerate in response to a RA microenvironment **(Tables 4 & 5).**

Both linear and 4-arm PEG-PLA copolymers were chosen to be assembled in a DMSO/water system. The ratio of water to DMSO is 20:1, which provides insufficient conditions for solvation with a larger entropic penalty, leading to rapid nucleation, limiting more complex morphologies from forming.

This ultimately results in small hydrophobic cores that limit morphologies to simple spherical aggregates.

$PLLA_{3.4K}$-PEG_{5K}-$PLLA_{3.4K}$ formulation (TB@MTX) (248 nm) formed a slightly smaller aggregate compared to 4-arm PEG_{5K}-$PLLA_{3.6K}$ formulation (4A@MTX) (250 nm), as the linear polymer's flexible chains can reorganize more freely in DMSO/water, forming larger spheres **(Figure 5).** In contrast, the 4-arm polymer's branched architecture results in a greater enthalpic penalty and cannot fold efficiently, which ultimately leads to larger aggregates.

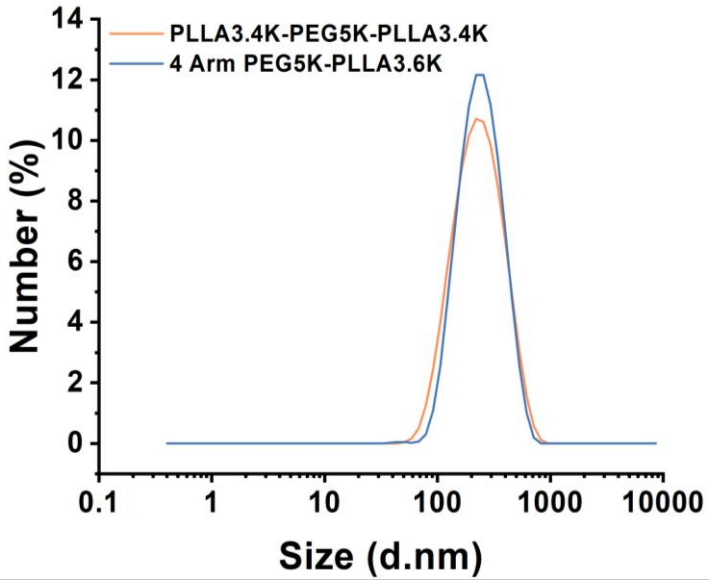

Figure 5. Dynamic light scattering graph of the size distribution of aggregates dispersed in solution.

With 5 mg (5,000 μg) of MTX being initially added to the formulations, there was a significant difference in the drug loading ability of each formulation. The four-arm polymer demonstrated better drug loading efficiency of 83.0% (4,150 μg loaded), while the triblock polymer achieved 73.3% efficiency (3,670 μg loaded). This represents a substantial difference of 483 μg more drug loaded in the four-arm formulation, exhibiting a 13.2% relative advantage.

3.3.2. Biocompatibility and Cytotoxicity

Once the formulations were created, the biocompatibility and cytotoxicity of these drug-loaded aggregates were investigated by hemolytic analysis and CCK8 measurements. Both of them provided evidence of the highly biocompatible nature of both 4A@MTX and TB@MTX. In various concentrations upwards of 1 mg/mL in hemolysis, all drugs had a hemolytic percentage of lower than 0.3% significantly lower than the 5% which is necessary for drug delivery carriers **(Figure 6a).** These findings suggest that the polymers can be safely used in vivo, but further studies are needed to assess the long-term biocompatibility and potential immune responses. The CCK8 measurements demonstrated a paradoxical relationship between drug concentration and cytotoxicity, which shows high drug concentration but low cytotoxicity. Its potential to promote cellular growth at higher concentrations shows promise to effectively reduce the number of dosages per month, as each administration can now carry elevated amounts of MTX **(Figure 6b).**

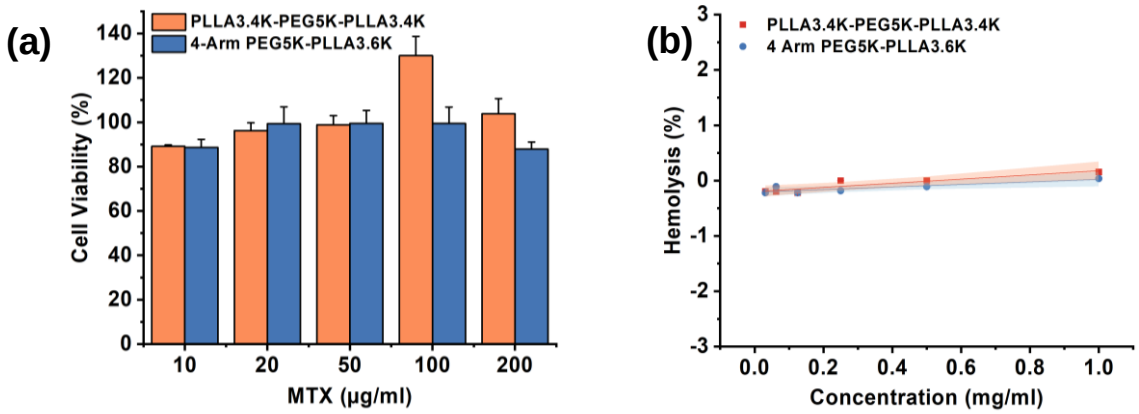

Figure 6. (a) Cell viability graph with different concentrations and carrier; (b) Hemolysis assay showing percentage of hemolysis with different concentrations.

3.3.3. Release Behavior

All formulations showed consistent release in all conditions over 48 h, with an initial burst release within the first hour, then transitioning to a gradual release. Over the time frame, no drug reaches complete release (100%), indicating good sustained release properties that could last longer and reduce the frequency of administration. Current MTX therapy typically requires weekly administration; these formulations could potentially extend dosing intervals, improving patient compliance and reducing administration-related side effects.

Notably, pH 6.5 conditions consistently showed increased release compared to the sample in pH 7.4. This suggests that lowered pH accelerates the release of MTX, likely due to the accelerated degradation of the formulation. The formulation formed from 4-arm PEG_{5K}-$PLLA_{3.6K}$ in pH 6.5 showed a 37.94% increase in the amount of MTX released over the 48-hour period. Similarly, $PLLA_{3.4K}$-PEG_{5K}-$PLLA_{3.4K}$ showed an increase of 35.20% as can be seen in **Figure 7a-b.** The slight increase in release from 4A@MTX may be attributed to its smaller size, which entails a greater SA/V ratio and its lower stability due to the architecture of the polymer.

Hydrogen peroxide (H_2O_2) significantly enhanced drug release under both pH conditions. At physiological pH 7.4, 4A@MTX released 42.87% faster in the presence of H_2O_2, while TB@MTX showed a 35.21% increase. Under acidic conditions (pH 6.5), the enhancement was somewhat reduced but still substantial, with 4-arm PEG_{5K}-$PLLA_{3.6K}$ and $PLLA_{3.4K}$-PEG_{5K}-$PLLA_{3.4K}$ formulations showing 18.70% and 19.08% faster release, respectively **(Figure 7a-b).**

The combination of acidic pH and H_2O_2 produced synergistic effects on drug release. When comparing release rates at pH 6.5 with H_2O_2 to those at pH 7.4 without H_2O_2, 4A@MTX released 63.73% faster, while TB@MTX showed a 61.00% increase, as seen in **Figure 7a-b**.

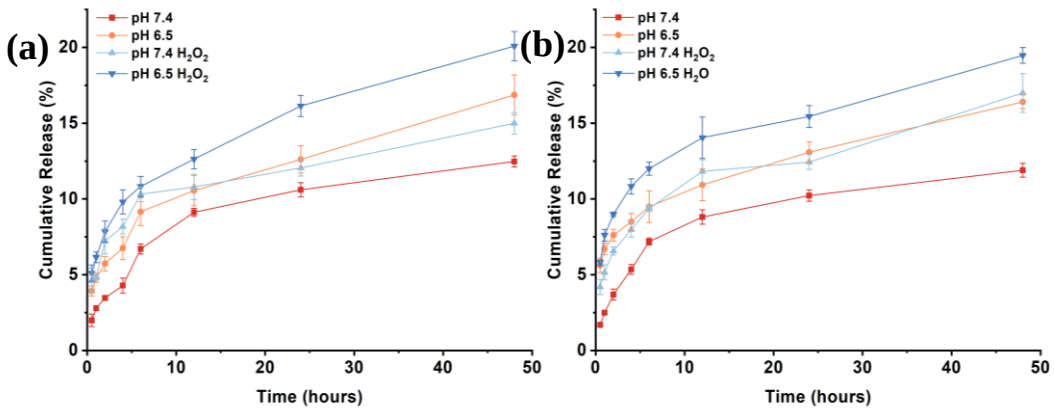

Figure 7. (a) TB@MTX cumulative release curve; (b) 4A@MTX cumulative release curve.

3.3.4. Therapeutic Effects

In order to confirm the efficacy of the designed nanoaggregates, ELISA, Western Blot, and confocal microscopy were utilized. The three Elisa graphs in **Figure 8** demonstrate the anti-inflammatory effects of the two formulations by measuring key inflammatory markers associated with RA. The data show measurements of TNF-α, IL-6, and IL-1β, all critical inflammatory cytokines that drive RA pathology. The experimental design compares healthy controls with LPS-induced inflammation, which serves as a disease model showing dramatically elevated inflammatory markers. Both the TB@MTX and 4A@MTX formulations demonstrate significant therapeutic effects, reducing TNF-α levels by approximately 60-65%, IL-6 by 50-60%, and IL-1β by 45-55% compared to the inflamed LPS group (**Figure 8a**). These results indicate a strong anti-inflammatory potential, suggesting that these formulations could provide effective management of RA symptoms. 4A@MTX is slightly more effective than TB@MTX across TNF-α and IL-6 inflammatory markers.

The Western blot graphs were created based on the luminosity of the proteins on the gel, assuming levels of actin are equal. 4A@MTX formulations showed the greater inhibition of VCAM-1 and NF-kB with 16.01% and 10.43% respectively. However, 4A@MTX showed a 6.42% lower inhibition in the PKB compared to TB@MTX, which is a very minor decrease compared to the inhibition of VCAM-1 and NF-kB resulting from TB@MTX (**Figure 8b**).

Additionally, based on the confocal microscopy after the LPS-induced inflammation, there was an increase in M1, indicating high inflammation. After the addition of 4A@MTX and TB@MTX, there is a substantial decrease in M1 polarization and a subsequent increase in M2 polarization, indicating high efficacy, corroborating the results from ELISA and Western Blot (**Figure 8c**).

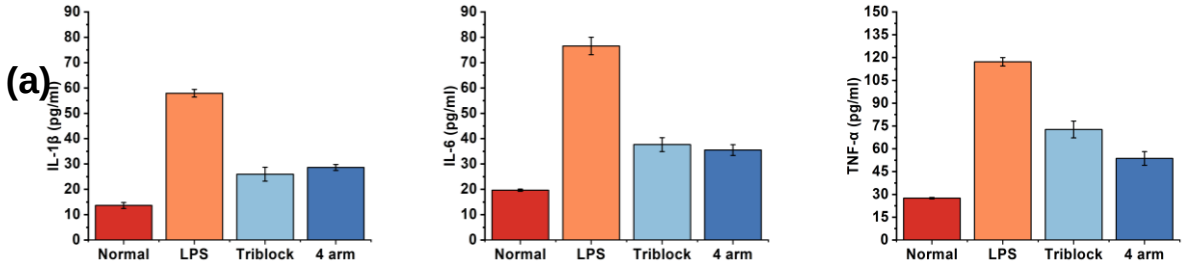

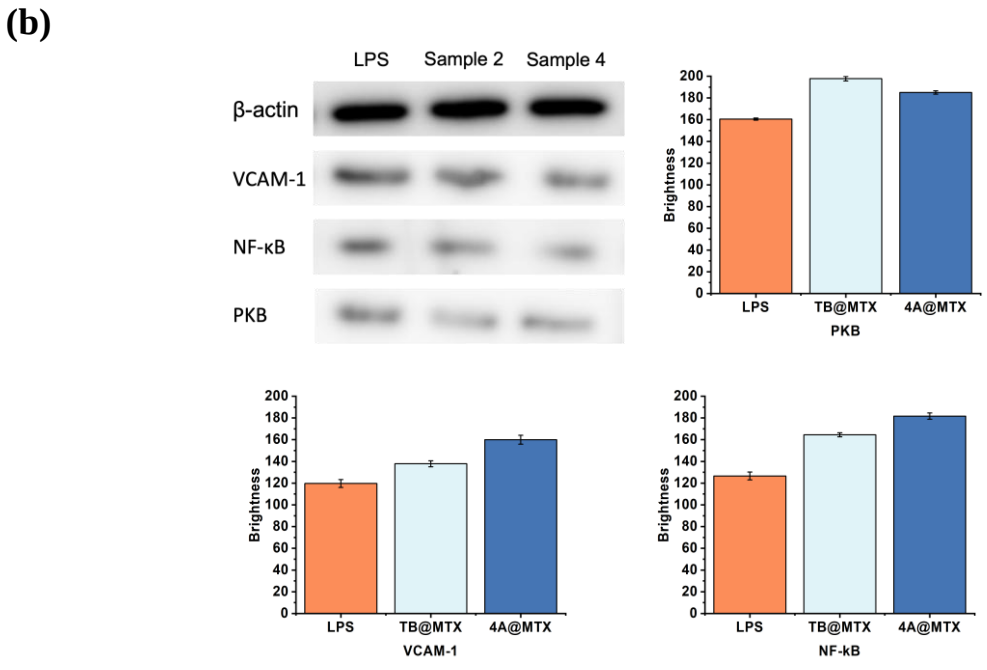

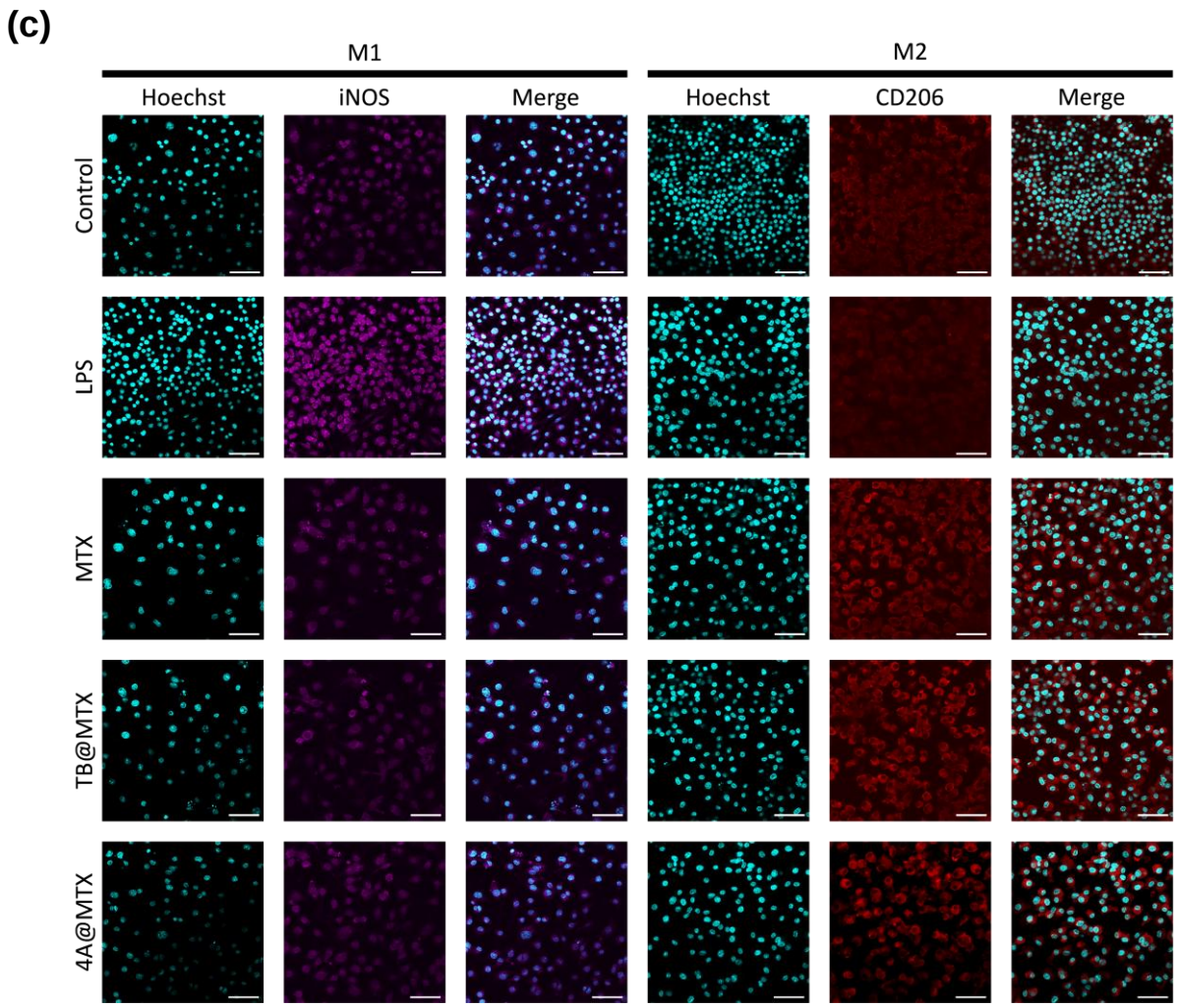

Figure 8. (a) ELISA quantification of inflammatory cytokines (IL-1β, TNF-α, and IL-6) across experimental conditions.
(b) Western blot analysis and quantification of inflammatory proteins, including VCAM-1, NF-κB, and p65, with β-actin as a control.
(c) Confocal microscopy analysis of macrophage polarization markers. Representative images showing M1 macrophages (iNOS-positive, purple) and M2 macrophages (CD206-positive, red/purple) under different treatment conditions. Nuclei were counterstained with Hoechst 33342 (cyan/blue). Scale bar: 50 μm.

4. Discussion

4.1. Effect of Block Ratio and Crystallinity

PLA chain length correlated positively with nanoaggregate size. For example, $PDLLA_{7.8K}$-PEG_{5K}-$PDLLA_{7.8K}$ forms spheres ranging from 200–700 nm, whereas shorter chains such as $PDLLA_{4.7K}$-PEG_{5K}-$PDLLA_{4.7K}$ form more uniform 100 nm spheres **(Table 2).** According to CPP theory, reducing PLA block length decreases hydrophobic volume and packing length, reducing aggregate size but not morphology, as the CPP value remains largely unchanged. Longer chains also introduce steric hindrance, preventing tight packing and favoring larger, more diverse morphologies.

Crystallinity further shaped morphology and size. PLLA's ability to crystallize allowed denser packing and more distinct structures, such as platelets in $PLLA_{6.8K}$-PEG_{5K}-$PLLA_{6.8K}$ (**Figure 1e)**. Higher crystallinity promoted morphological diversity (rings, cylinders, dumbbells) but reduced size by improving packing efficiency.

4.2. Effect of Polymer Architecture

Polymer architecture strongly influenced morphology. Linear PLA-*b*-PEG mainly formed simple spheres or platelets, while four-arm PEG-PLLA generated larger, more complex aggregates (e.g., dumbbells and cylinders). Steric hindrance in branched systems limited compact packing, favoring non-spherical shapes. CPP theory explains this: increasing PLA arm number enlarges hydrophobic volume, raising CPP and promoting lamellar or cylindrical morphologies **(Figures 1d-e)**.

4.3. Effect of Solvent and PDI

Solvent choice critically affected self-assembly. Poorer solvents like dioxane enhanced hydrophobic effects, accelerating nucleation and yielding smaller aggregates (50–200 nm). In contrast, THF solvated PLA more effectively, slowing nucleation and favoring larger structures (300–700 nm). These results align with LaMer's nucleation–growth model.

PDI also impacted uniformity: linear copolymers with narrow distributions produced monodisperse structures, whereas multi-arm copolymers with higher PDI generated heterogeneous aggregates. Overall, PDLLA tended to form larger, more diverse structures, while PLLA produced smaller, denser aggregates.

4.4. Drug Loading and Release

Morphology dictated surface area-to-volume ratio (SA/V) and drug loading. Platelets showed higher SA/V than spheres, explaining PLLA6.8K's superior loading (16.51%). Smaller spheres (e.g., $PDLLA_{4.7K}$-PEG_{5K}-$PDLLA_{4.7K}$) also enabled efficient loading. Solvent choice influenced chain extension, further affecting capacity.

Release kinetics revealed molecular weight effects: longer PLA chains slowed release in linear copolymers (lower k values, **Tables 3 & 4**), while 4-arm copolymers showed the opposite trend, likely due to steric crowding and destabilized micellar cores. Crystallinity and drug–polymer interactions also modulated release, though less strongly. Longer PLA chains increased diffusion coefficients by creating complex morphologies and new degradation pathways.

4.5. Outliers and Design Framework

The 4-arm PEG_{5K}-$PLLA_{12.6K}$ copolymer is an outlier, showing low loading but high release. Likely explanations include drug adsorption onto PEG shells and rigid crystalline cores restricting loading but stabilizing release. Despite its high molecular weight, it also formed unusually small aggregates, possibly due to high nucleation rates and a lower polymer count per solution. These findings highlight the importance of matching morphology with therapeutic needs: spherical aggregates, with higher surface area-to-volume ratios, are more suitable for rapid release in acute treatment, whereas platelets or cylindrical aggregates enable slower and more sustained release, making them better suited for chronic suppression. In this way, the observed structure–property relationships support a retrosynthetic design framework that can guide the rational selection of copolymers for specific clinical applications.

4.6. Validation and Comparative Performance

The 44A@MTX formulation achieved higher drug loading (83% vs. 73% for TB@MTX) and strong anti-inflammatory efficacy (45–65% cytokine reduction). Compared with other systems (e.g., cross-linked copolymers or IHTM), our carriers achieved similar or superior responsiveness under physiologically relevant ROS/pH conditions. Notably, the 63.73% faster release under combined pH 6.5/H_2O_2, which is both at a higher pH and lower concentration of H_2O_2 compared to previous studies, validates the potential of utilizing ROS and pH as an activator of accelerated and targeted release to suppress inflammatory responses resulting from RA.

The branched architecture not only improved drug loading but also enhanced responsiveness to inflammatory triggers, with superior inhibition of VCAM-1 and NF-κB pathways. While PLGA-hyaluronic acid nanoparticles can achieve 95.2% encapsulation,our PLA-*b*-PEG system offers advantages in design simplicity and scalability.[21]

5. Conclusion

This study highlights the significant role of polymer architecture in the self-assembly of PLA-*b*-PEG block copolymers. The number of arms in the polymer influences morphological complexity, drug-loading efficiency, and release kinetics. These analyses of these findings were used to create a framework for the design of PLA-*b*-PEG based drug delivery carriers. However, caution is needed when applying these patterns to design novel drug delivery systems due to the limited sample variations in this study. While certain behavioral patterns were observed, some of the underlying mechanisms remain unclear, requiring further research.

Additionally, in this study, we successfully developed and characterized 2 selected PLA-*b*-PEG-based polymers for targeted drug delivery systems for RA. Both $PLLA_{3.4K}$-PEG_{5K}-$PLLA_{3.4K}$ and 4-arm PEG_{5K}-$PLLA_{3.6K}$ formulations exhibited favorable drug loading efficiencies and predictable release profiles, suggesting their potential for clinical applications. The synergistic effects of acidic conditions with ROS, like hydrogen peroxide, show enhanced drug release, highlighting its capabilities to reduce acute RA through accelerated targeted delivery, and the sustained release underscores its ability to suppress RA once the acute release period is over and inflammatory responses weaken. Furthermore, the significant reduction in key inflammatory markers underscores the therapeutic promise of these polymers in mitigating inflammation associated with RA.

Future research will focus on exploring the in vivo performance of 4A@MTX by assessing its long-term stability and investigating potential immune responses. Ultimately, this work lays the groundwork for the development of innovative drug delivery systems that can improve patient outcomes.

References

[1] Y. Zhu et *al.*, "Rheumatoid arthritis microenvironment insights into treatment effect of nanomaterials," *Nano Today*, vol. 42, p. 101358, 2022/02/01/ 2022, doi: https://doi.org/10.1016/j.nantod.2021.101358.

[2] V. Di Francesco, M. Di Francesco, P. Decuzzi, R. Palomba, and M. Ferreira, "Synthesis of Two Methotrexate Prodrugs for Optimizing Drug Loading into Liposomes," (in eng), *Pharmaceutics*, vol. 13, no. 3, Mar 4 2021, doi: 10.3390/pharmaceutics13030332.

[3] K. M. Hamed *et al.*, "Overview of Methotrexate Toxicity: A Comprehensive Literature Review," (in eng), *Cureus*, vol. 14, no. 9, p. e29518, Sep 2022, doi: 10.7759/cureus.29518.

[4] L. Guo, S. Zhong, P. Liu, M. Guo, J. Ding, and W. Zhou, "Radicals Scavenging MOFs Enabling Targeting Delivery of siRNA for Rheumatoid Arthritis Therapy," *Small*, vol. 18, no. 27, p. 2202604, 2022, doi: https://doi.org/10.1002/smll.202202604.

[5] H. S. Han and K. Y. Choi, "Advances in Nanomaterial-Mediated Photothermal Cancer Therapies: Toward Clinical Applications," (in eng), *Biomedicines*, vol. 9, no. 3, Mar 16 2021, doi: 10.3390/biomedicines9030305.

[6] S. Senapati, A. K. Mahanta, S. Kumar, and P. Maiti, "Controlled drug delivery vehicles for cancer treatment and their performance," *Signal Transduction and Targeted Therapy*, vol. 3, no. 1, p. 7, 2018/03/16 2018, doi: 10.1038/s41392-017-0004-3.

[7] W. Zhang and A. H. E. Müller, "Architecture, self-assembly and properties of well-defined hybrid polymers based on polyhedral oligomeric silsequioxane (POSS)," *Progress in Polymer Science*, vol. 38, no. 8, pp. 1121-1162, 2013/08/01/ 2013, doi: https://doi.org/10.1016/j.progpolymsci.2013.03.002.

[8] S. Venkataraman *et al.*, "The effects of polymeric nanostructure shape on drug delivery," *Advanced Drug Delivery Reviews*, vol. 63, no. 14, pp. 1228-1246, 2011/11/01/ 2011, doi: https://doi.org/10.1016/j.addr.2011.06.016.

[9] N. Hoshyar, S. Gray, H. Han, and G. Bao, "The Effect of Nanoparticle Size on In Vivo Pharmacokinetics and Cellular Interaction," *Nanomedicine*, vol. 11, no. 6, pp. 673-692, 2016/03/01 2016, doi: 10.2217/nnm.16.5.

[10] M. J. Mitchell, M. M. Billingsley, R. M. Haley, M. E. Wechsler, N. A. Peppas, and R. Langer, "Engineering precision nanoparticles for drug delivery," *Nature Reviews Drug Discovery*, vol. 20, no. 2, pp. 101-124, 2021/02/01 2021, doi: 10.1038/s41573-020-0090-8.

[11] S. Shen, Y. Wu, Y. Liu, and D. Wu, "High drug-loading nanomedicines: progress, current status, and prospects," (in eng), *Int J Nanomedicine*, vol. 12, pp. 4085-4109, 2017, doi: 10.2147/ijn.S132780.

[12] Y. Mai and A. Eisenberg, "Self-assembly of block copolymers," *Chemical Society Reviews*, 10.1039/C2CS35115C vol. 41, no. 18, pp. 5969-5985, 2012, doi: 10.1039/C2CS35115C.

[13] C. J. Rijcken, T. F. Veldhuis, A. Ramzi, J. D. Meeldijk, C. F. van Nostrum, and W. E. Hennink, "Novel fast degradable thermosensitive polymeric micelles based on PEG-block-poly(N-(2-hydroxyethyl)methacrylamide-oligolactates)," (in eng), *Biomacromolecules*, vol. 6, no. 4, pp. 2343-51, Jul-Aug 2005, doi: 10.1021/bm0502720.

[14] D. Bobo, K. J. Robinson, J. Islam, K. J. Thurecht, and S. R. Corrie, "Nanoparticle-Based Medicines: A Review of FDA-Approved Materials and Clinical Trials to Date," (in eng), *Pharm Res*, vol. 33, no. 10, pp. 2373-87, Oct 2016, doi: 10.1007/s11095-016-1958-5.

[15] A. Pan, A. K. Rakshit, and S. P. Moulik, "Micellization thermodynamics and the nature of enthalpy–entropy compensation," *Colloids and Surfaces A: Physicochemical and Engineering Aspects*, vol. 495, pp. 248-254, 2016/04/20/ 2016, doi: https://doi.org/10.1016/j.colsurfa.2016.02.007.

[16] A. Vlachopoulos *et al.*, "Poly(Lactic Acid)-Based Microparticles for Drug Delivery Applications: An Overview of Recent Advances," (in eng), *Pharmaceutics*, vol. 14, no. 2, Feb 4 2022, doi: 10.3390/pharmaceutics14020359.

[17] P. J. Hurst, A. M. Rakowski, and J. P. Patterson, "Ring-opening polymerization-induced crystallization-driven self-assembly of poly-L-lactide-block-polyethylene glycol block copolymers (ROPI-CDSA)," *Nature Communications*, vol. 11, no. 1, p. 4690, 2020/09/17 2020, doi: 10.1038/s41467-020-18460-2.

[18] Z. Wang, Y. Cao, J. Song, Z. Xie, and Y. Wang, "Cooperation of Amphiphilicity and Crystallization for Regulating the Self-Assembly of Poly(ethylene glycol)-block-poly(lactic acid) Copolymers," *Langmuir*, vol. 32, no. 37, pp. 9633-9639, 2016/09/20 2016, doi: 10.1021/acs.langmuir.6b02211.

[19] R. Liu, Z. Rong, G. Han, X. Yang, and W. Zhang, "Synthesis and self-assembly of star multiple block copolymer of poly(4-vinylpyridine)-block-polystyrene," *Polymer*, vol. 215, p. 123431, 2021/02/12/ 2021, doi: https://doi.org/10.1016/j.polymer.2021.123431.

[20] R. López-Ríos de Castro, R. M. Ziolek, and C. D. Lorenz, "Topology-controlled self-assembly of amphiphilic block copolymers," *Nanoscale*, 10.1039/D3NR01204B vol. 15, no. 37, pp. 15230-15237, 2023, doi: 10.1039/D3NR01204B.

[21] R. M. Trujillo-Nolasco *et al.*, "Preparation and in vitro evaluation of radiolabeled HA-PLGA nanoparticles as novel MTX delivery system for local treatment of rheumatoid arthritis," *Materials Science and Engineering: C*, vol. 103, p. 109766, 2019/10/01/ 2019, doi: https://doi.org/10.1016/j.msec.2019.109766.